Growth and Characterization of Pyrite Thin Films for Photovoltaic Applications

by

Alex Wertheim

A Thesis Presented in Partial Fulfillment
of the Requirements for the Degree
Masters of Science

Approved November 2014 by the
Graduate Supervisory Committee:

Nathan Newman, Chair
Rakesh Singh
Mariana Bertoni

ARIZONA STATE UNIVERSITY

December 2014

ABSTRACT

A series of pyrite thin films were synthesized using a novel sequential evaporation technique to study the effects of substrate temperature on deposition rate and micro-structure of the deposited material. Pyrite was deposited in a monolayer-by-monolayer fashion using sequential evaporation of Fe under high vacuum, followed by sulfidation at high S pressures (typically > 1 mTorr to 1 Torr). Thin films were synthesized using two different growth processes; a one-step process in which a constant growth temperature is maintained throughout growth, and a three-step process in which an initial low temperature seed layer is deposited, followed by a high temperature layer, and then finished with a low temperature capping layer. Analysis methods to analyze the properties of the films included Glancing Angle X-Ray Diffraction (GAXRD), Rutherford Back-scattering Spectroscopy (RBS), Transmission Electron Microscopy (TEM), Secondary Ion Mass Spectroscopy (SIMS), 2-point IV measurements, and Hall effect measurements. Our results show that crystallinity of the pyrite thin film improves and grain size increases with increasing substrate temperature. The sticking coefficient of Fe was found to increase with increasing growth temperature, indicating that the Fe incorporation into the growing film is a thermally activated process.

ACKNOWLEDGEMENTS

TABLE OF CONTENTS

LIST OF TABLES

LIST OF FIGURES

CHAPTER 1

INTRODUCTION

INVESTMENT IN PHOTOVOLTAIC TECHNOLOGY

According to Ellaban et al, [1] U.S. photovoltaic (PV) capacity increased at an average annual growth rate of 60% up to 2012. In the same year, a total of $140 billion was spent installing PV technology in the U.S. and PV energy production reached ~2.5 GW globally. It is expected that the increased use of PV production will continue in the U.S. and world-wide, towards a global PV capacity in terawatts in the coming decades. To realize this important advancement in clean and renewable energy, the cost and environmental impact of this technology need to be minimized.

SEMICONDUCTORS FOR TERAWATT-SCALE PHOTOVOLTAICS

Currently, the push towards terawatt scale PV is largely limited by the high costs involved in producing high purity semiconductors [2]. While Si based PV cells boast efficiencies between 10-15% their cost effectiveness is limited by the expense of purifying the raw materials. Other semiconductors used in PV systems, including GaAs, $CuInGeSe_2$ (CIGS), and CdTe, boast similar or higher efficiencies. However they all contain costly, relatively rare, and toxic elements [2]. Thus, to achieve the terawatt goal, materials for the next generation of low-cost, large-area solar cells need to be found that are abundant, and inexpensive to purify and deposit in usable form.

Pyrite (FeS_2) is a a potentially important candidate for development of terawatt-scale PV technology. Pyrite's band gap of 0.95 eV is desirable for both single and tandem cells. Fe and S are non-toxic, environmentally benign and pyrite's high absorption coefficient (~$5x10^{-5}$ cm^{-1} at wavelengths less than 750 nm) is 2 orders of magnitude larger than Si [2, 3], making it possible to absorb over 90% of the absorbable light using less than 0.1 μm thick pyrite layers. The

abundance and ease of purification of Fe and S make pyrite attractive from an economic standpoint. In a recent study of 23 solar cell material candidates, pyrite was ranked first based on its natural abundance, and is further desirable due to minimal layer thickness required to fabricate PV devices and maximize potential energy output[2, 3, 4]. Figure 1 shows a comparison of the amount of photo-current that can be generated by the absorption of light in layers of pyrite and Si of comparable thickness.
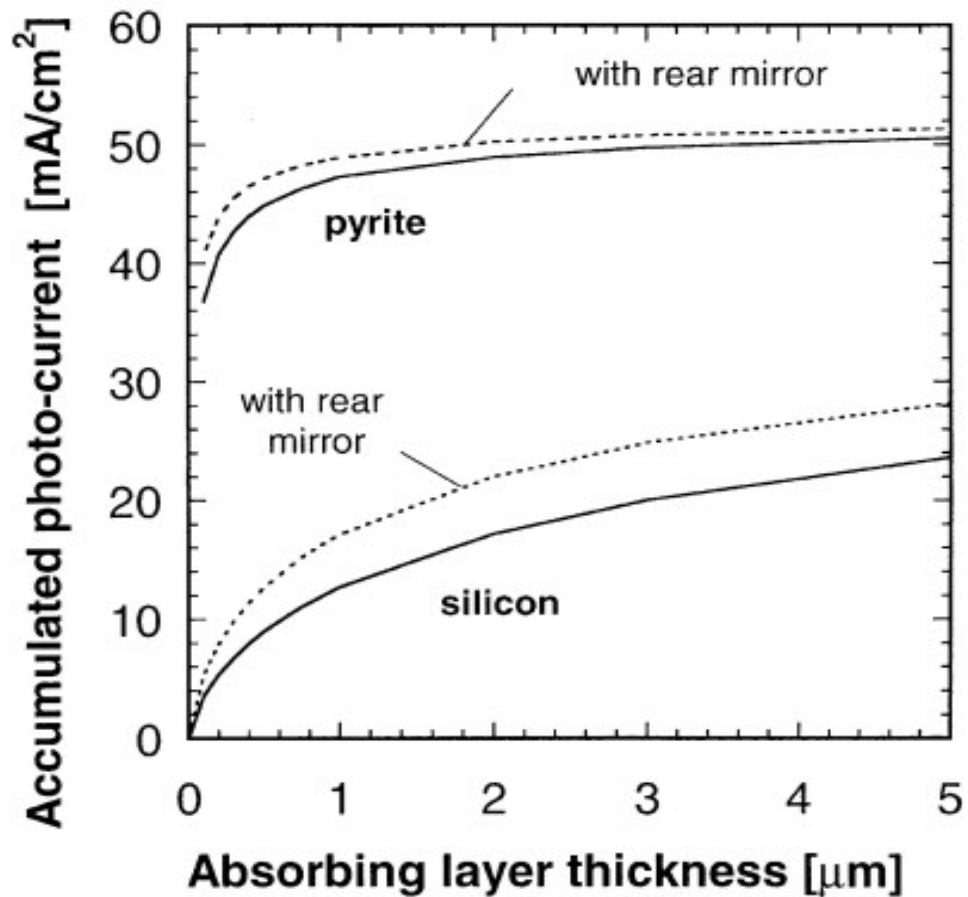

Fig 1: Simulation results of photo-current generated by layers as a function of thickness for Si and pyrite. Dashed lines indicate that a rear reflector was included in the simulation. [3]

EXISTING PYRITE SYNTHESIS METHODS

There has been a large number of studies aimed at developing methods for the synthesis of pyrite thin films. Growth methods involving chemical vapor based synthesis, including Metal Organic Chemical Vapor Deposition (MOCVD), produce high quality pyrite films, but require the use of expensive chemical precursors [5, 6, 7]. Pyrite films synthesized via sputtering could only achieve single phase stoichiometric pyrite at low substrate temperatures of ~75ºC [8]. MBE has been used to synthesize pyrite at substrate temperatures up to 300ºC, although the studies have been limited to relatively low sulfur pressures of ~10^{-6} Torr [9]. The low substrate temperatures and sulfur pressures used in the sputtering and MBE studies were not able to produce low-defect pyrite films with sufficiently-long carrier lifetimes and large diffusion lengths [8]. While physical vapor deposition (PVD) synthesis techniques are simple and low cost, they have not been able to produce pyrite thin films with sufficiently high crystal quality for PV applications.

In a previous study conducted by this research group, Vahidi et al [10] were able to produce single phase polycrystalline pyrite thin films grown on Si, as well as epitaxial pyrite grown on natural pyrite substrates. To carry out this work, they invented a device in which the substrates are rotated cyclically between Fe deposition at low sulfur pressures, followed by sulfidation at high sulfur pressures (Fig 2). Their work showed that kinetic barriers to the forward reaction was the rate limiting step in pyrite films grown by PVD. The pyrite films initially fabricated with this technique were topographically rough and often discontinuous.
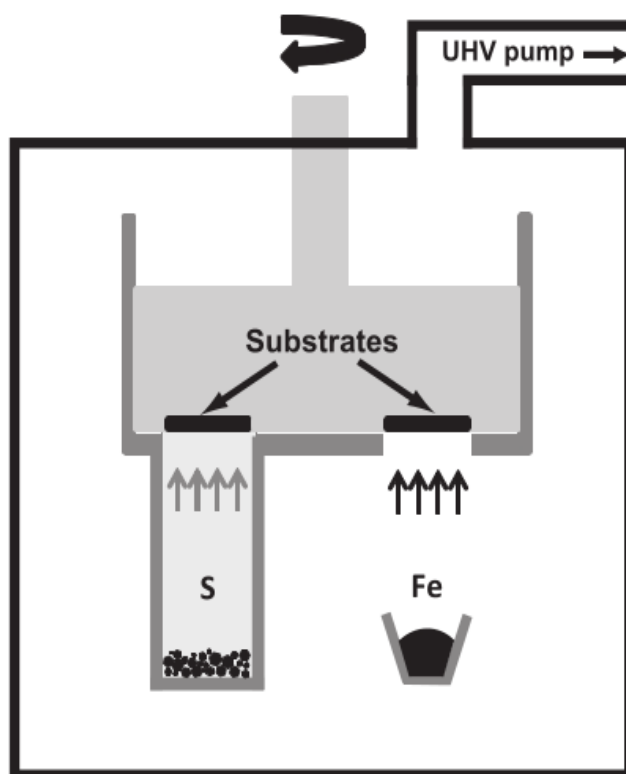
Figure 2: Schematic of Sequential Evaporation method [10].

PRESENT WORK

The work presented here continued the efforts of Vahidi et al with the goal of optimizing the thin film morphology. I modified the growth apparatus and developed new procedures to improve the control of the sequential evaporation growth conditions, including the impinging S and Fe rates and the substrate temperature. Then, to investigate the role of growth conditions on topographic, electrical, chemical and structural characteristics, I grew films with two different growth sequences. In the first one, I maintained a constant substrate temperature during growth, and in the second I grew a low temperature buffer layer, a higher temperature layer and then a low temperature capping layer. I then characterized the films to better understand the influence of growth conditions on film properties.

CHAPTER 2

EXPERIMENTAL METHODS

SYNTHESIS CHAMBER

The UHV system is pumped by a ~60 L/s turbo-molecular vacuum pump and reaches an unbaked base pressure of ~1.5×10^{-5} Torr, with the background pressure comprised of predominantly residual S gas. The substrate temperature is controlled using a programmable temperature controller in conjunction with a type-K thermocouple. In this study, the S crucible, filled with 99.999% pure (Alpha Aesar) S granules, was maintained at 147 ± 2°C during growth, corresponding to a S pressure of ~100 mTorr. Fe was evaporated from an alumina coated W crucible filled with 99.98% pure (Alpha Aesar) Fe granules. The Fe evaporation rate was kept constant. The substrate rotation rate was ~5 revolutions per minute. A pressure of ~5×10^{-4} Torr or lower in the main chamber was maintained during growth.

SUBSTRATE PREPARATION

Films were deposited on single crystal Si[100], thermal oxide buffered Si (i.e. SiO_2), and sapphire substrates during each experiment. Si and pyrite both have cubic structure and are latticed matched to within 0.2%, suggesting epitaxial pyrite films on Si are possible. All substrates were initially cleaned by ultrasonication in semiconductor grade acetone for 5 minutes and isopropanol for 5 minutes, followed by a DI water rinse and immediately blown off with dry N_2. Si[100] substrates were dipped in HF diluted to 5% in DI water for 3 minutes to etch the native oxide and then placed into the UHV chamber within 15 minutes for the growth experiment.

GROWTH PROCESSES

Thin film synthesis was performed using two different growth sequences. The first utilized a single-step process with constant substrate temperatures, between 250°C and 450°C, lasting for 90 minutes, followed by a 30 minute in-situ anneal (Fig 3A). The second growth sequence was

5

a three-step process (Fig 3B). (1) For the first 20 minutes of each growth experiment the substrates were heated to a temperature between 100ºC and 300ºC to form a seed layer. (2) The substrate temperature was then quickly increased by 150ºC (ramping takes between 3-5 minutes) and kept at the higher temperature for another 20 minutes. (3) With substrate rotation and evaporation continuing, the substrates were allowed to cool down naturally to within approximately 15ºC of the temperature used to deposit the seed layer. Upon reaching the lower temperature, growth continued for another 20 minutes to deposit a capping layer. Fe evaporation was then terminated and both the substrate temperature and S pressure were maintained for 30 minutes to perform an in-situ anneal. Total growth times were kept as close as possible to 90 minutes. Longer growth times were inevitable due to slower cool down rate at lower temperatures. In both one-step and three-step processes, S pressure was maintained at ~100 mTorr throughout each growth by maintaining a constant S crucible temperature of 147ºC.

ANALYSIS TECHNIQUES

Glancing Angle X-Ray Diffraction (GAXRD) is performed to identify primary and secondary phases present and to quantify crystal quality in the deposited films. Rutherford Back-scattering Spectroscopy (RBS) is performed to measure stoichiometry and thickness, as well as to identify contaminants and determine their concentration. Secondary-Ion Mass Spectroscopy (SIMS) was performed on some films to monitor trace contaminants. Transmission electron microscopy (TEM) were used to image the film morphology and crystal structure. Temperature-dependent Hall and resistivity measurements were performed in the Van Der Pauw configuration with pressed In ohmic contacts on films grown on SiO_2 substrates to determine resistivity, electronic carrier concentration, carrier type and mobility.
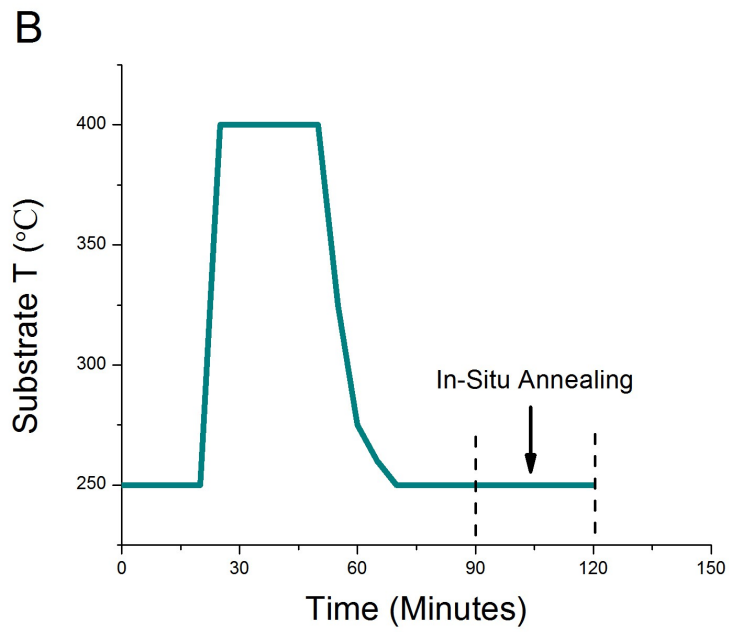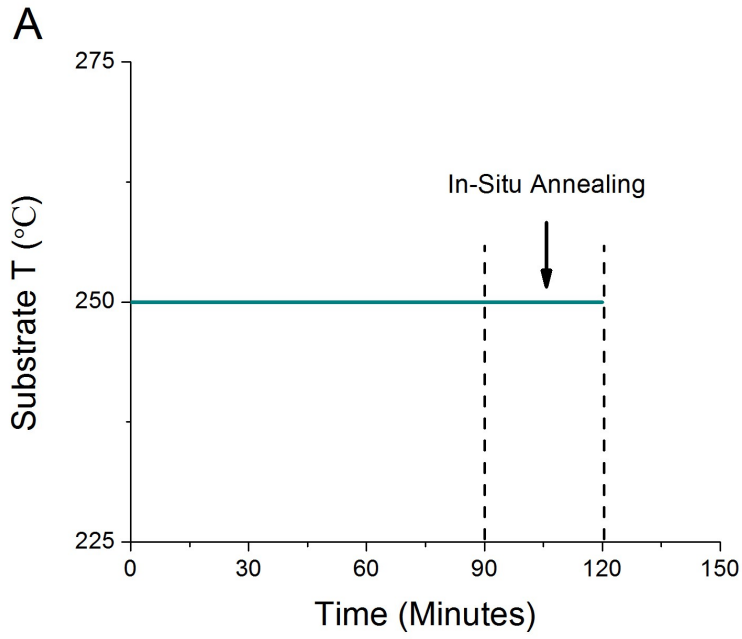
Figure 3: Examples of temperature cycles used during growth. A): one-step substrate temperature processes and B): three-step substrate temperature processes.

CHAPTER 3

RESULTS & DISCUSSION

STRUCTURAL CHARACTERIZATION

In our experiments, Fe evaporation alone in the chamber's large residual background S pressure is found to form FeS. Therefore the ambient S gas reacts with Fe to form an FeS species in the first chamber region where the sample is exposed to Fe evaporation and then it is fully reacted to form pyrite in the chamber region which contains only S. A number of studies have concluded that the formation of pyrite first involves the formation of FeS, followed by the reaction with an addition S atom to form FeS_2 [11, 12].

All results discussed in this section were found in films grown on Si[100]. Growths utilizing the single-step and three-step growth processes were found to be single phase polycrystalline pyrite (Figs. 4A & 4B). Judging from the full width at half maximum (FWHM) of the GAXRD peaks, it is evident that crystallinity improves with increasing substrate temperature (Figs. 5A & 5B). Films grown in a one-step process all have the stoichiometric pyrite S to Fe ratio of 2:1. In contrast, some films grown at higher temperatures with the three-stage process possess up to 5% higher S to Fe ratio (Fig 6).

8
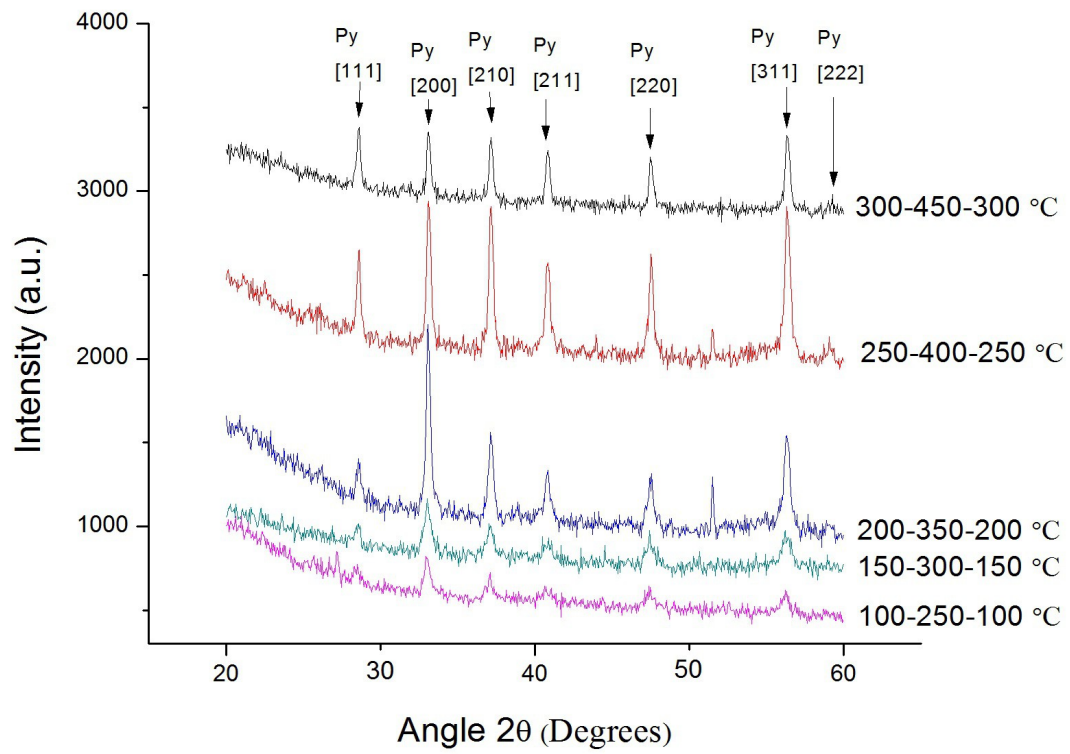
Figure 4A: Glancing Angle X-Ray Diffraction patterns of 5 samples grown with a three-step temperature cycle. "Py" indicates pyrite phase peaks.

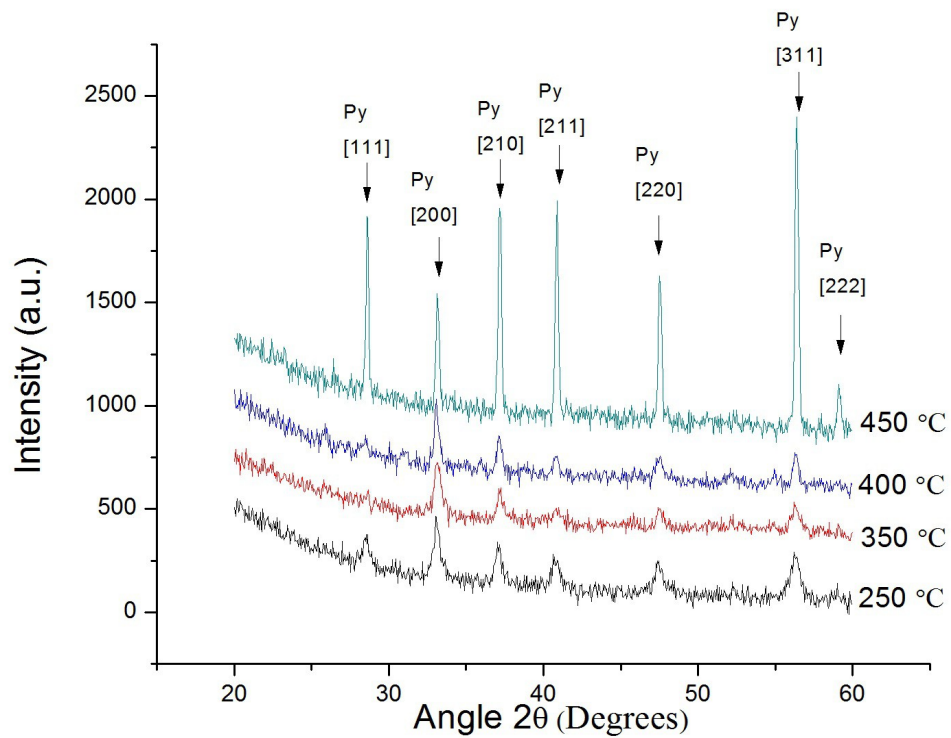Figure 4B: Glancing Angle X-Ray Diffraction patterns of 4 samples grown with a one-step

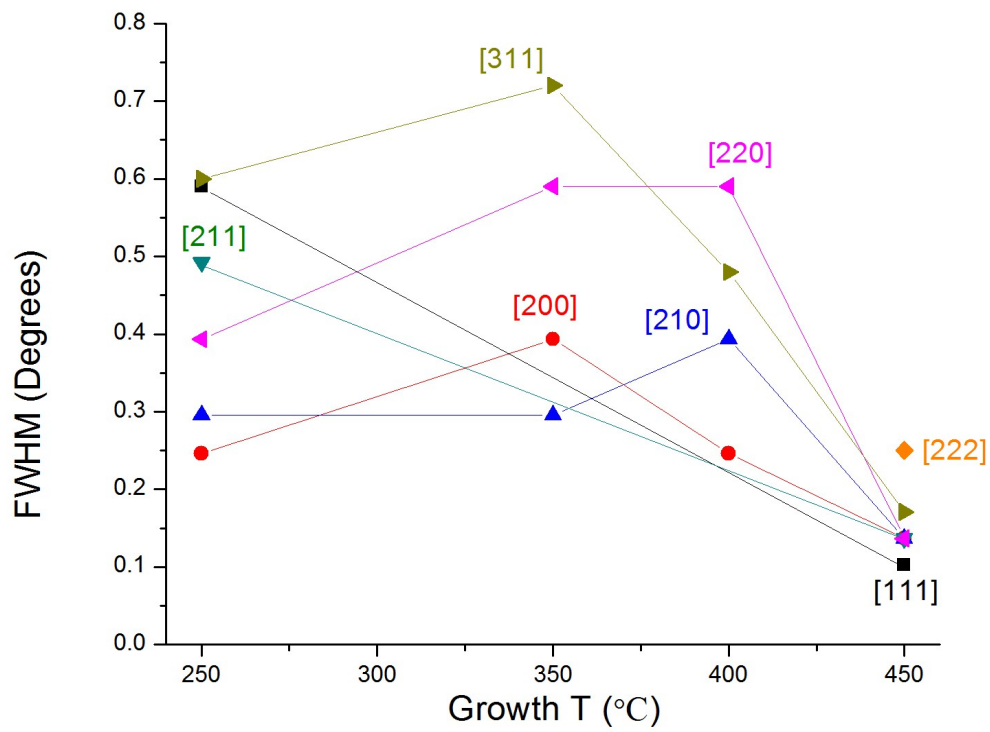temperature cycle. "Py" indicates pyrite phase peaks.

Figure 5A: FWHM vs higher growth temperature of the three-step temperature cycle
growths. Each pyrite crystal plane is represented as its own trend.
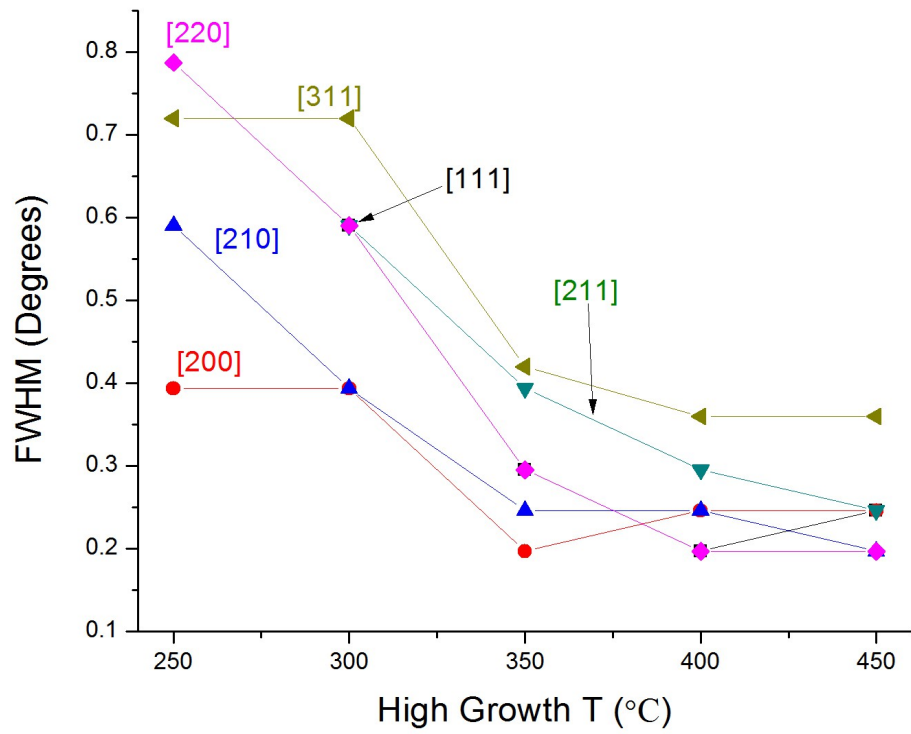
Figure 5B: FWHM vs growth temperature of the one-step temperature cycle growths.

Each pyrite crystal plane is represented as its own trend.
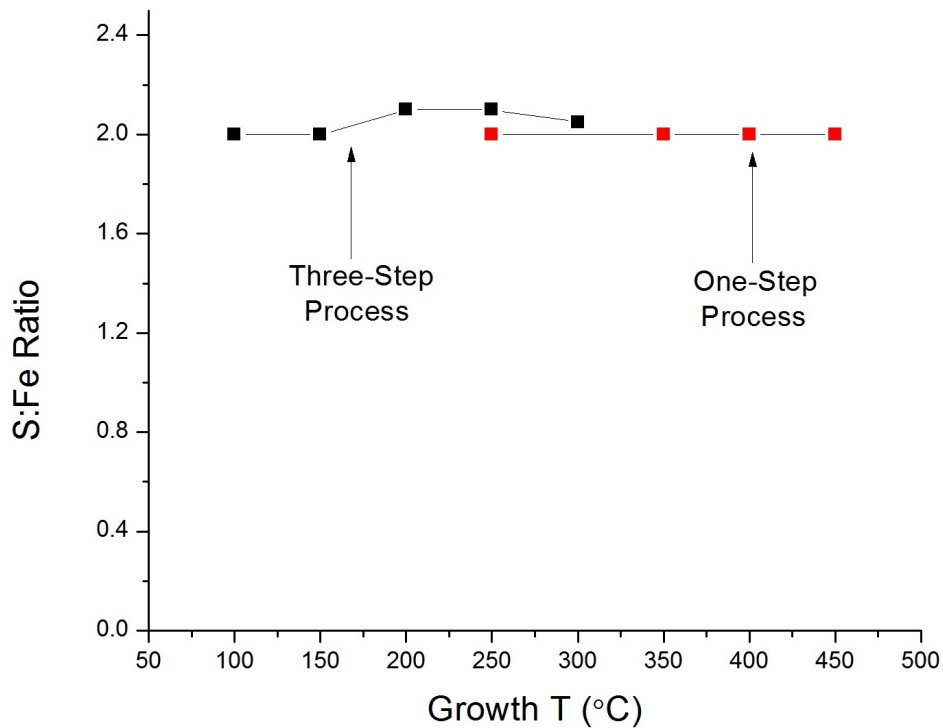
Figure 6: S to Fe ratio of three-step and one-step growths.

At a constant Fe deposition rate, the film growth rate increased monotonically with substrate temperature (Fig 7). The one-step growths at 250ºC and 450ºC showed an increasing trend in growth rate. The small Fe sticking coefficient at lower substrate temperatures is surprising. Given that, at 450ºC, elemental Fe has a vapor pressure of $<10^{-9}$ Torr (Fig 8), and the evaporated Fe gas sticks to most other known surfaces. This indicates that Fe or an iron sulfide precursor species evaporates from the surface during growth and is not from the decomposition of the fully reacted FeS_2 pyrite phase.

In a study by G. Kullerud et al (1959), evacuated glass tubes containing pyrite and pyrrhotite (FeS) were heated to temperatures up to 800ºC to study the thermal decomposition process. Quenching the heated tubes resulted in the condensation of S gas produced by the decomposition of the Fe-S system. In an analysis of this condensation, the deposits were found to contain mostly S and as much as 0.1 weight % Fe [13]. At this temperature and for Fe:S ratios of <1, the ratio of Fe:S in the vapor under these conditions would be expected to be ~10^{-7} (Fig 8). Although the Kullerud experiments suggest that an Fe-containing species may evolve at a faster rate than expected from thermodynamics alone, not enough detail about the ratio of the total amount of Fe and S used in their experiments is provided to give definitive answers. To understand the thermochemical factors involved in the low sticking coefficient in our work, additional experiments are needed. Measurements of the gas content over pyrite and pyrrhotite surfaces in a closed system will provide the needed thermodynamic parameters. To determine if kinetic barriers play a role, evaporation experiments in steady state (i.e. in an open system) should be done to measure the evaporation rate of each species desorbed from Fe and pyrrhotite surfaces.

The growth rates of thin films synthesized with a one-step process as a function of growth temperature are summarized in Fig 9. The slope of the Arrhenius graph ($\Delta H/k_B T$) was used to infer the enthalpy of formation where, where ΔH is the enthalpy of formation and k_B is the Boltzmann constant. The measured enthalpy, $\Delta H = 1.56 \times 10^{-1}$ eV, suggests that the rate limiting step is from a kinetic barrier from a surface process involving Fe physisorption, surface diffusion or reaction at a terrace, kink, ledge or other surface feature.
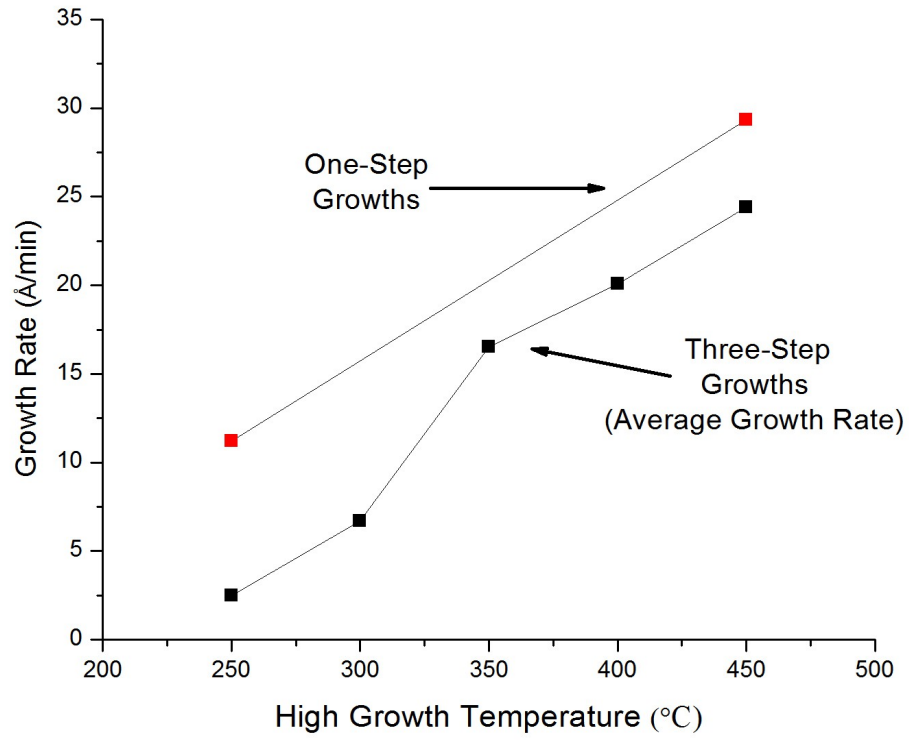
Fig 7: Growth rate of pyrite thin films as a function of the highest growth temperature of the three-step cycle. One-step growths were repeated at highest and lowest temperatures to verify this trend.
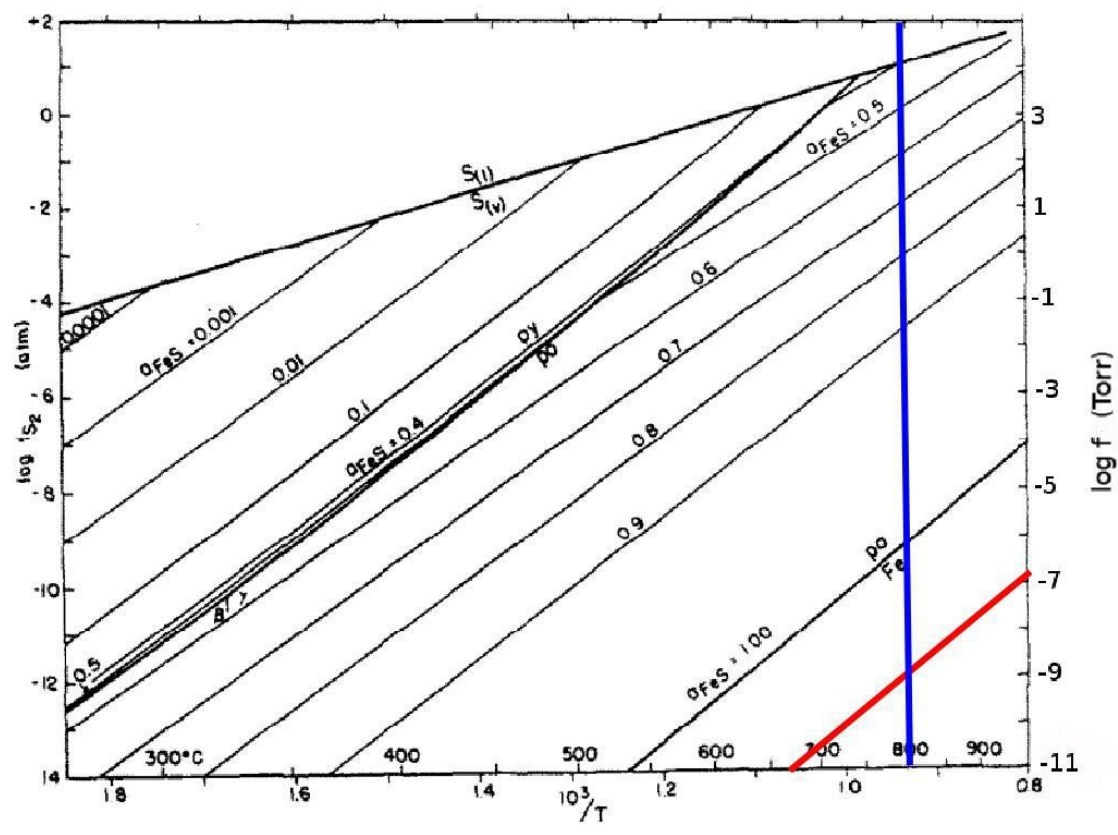
Figure 8: Equilibrium fugacity of S_2 from the Fe-S system as a function of temperature [11, 12]. Red line: Fugacity of Fe from bulk Fe. Blue line: displays all values at 800ºC.

$-\Delta H/k_B = -792$ K

$\Delta H = 1.56 \times 10^{-1}$ eV
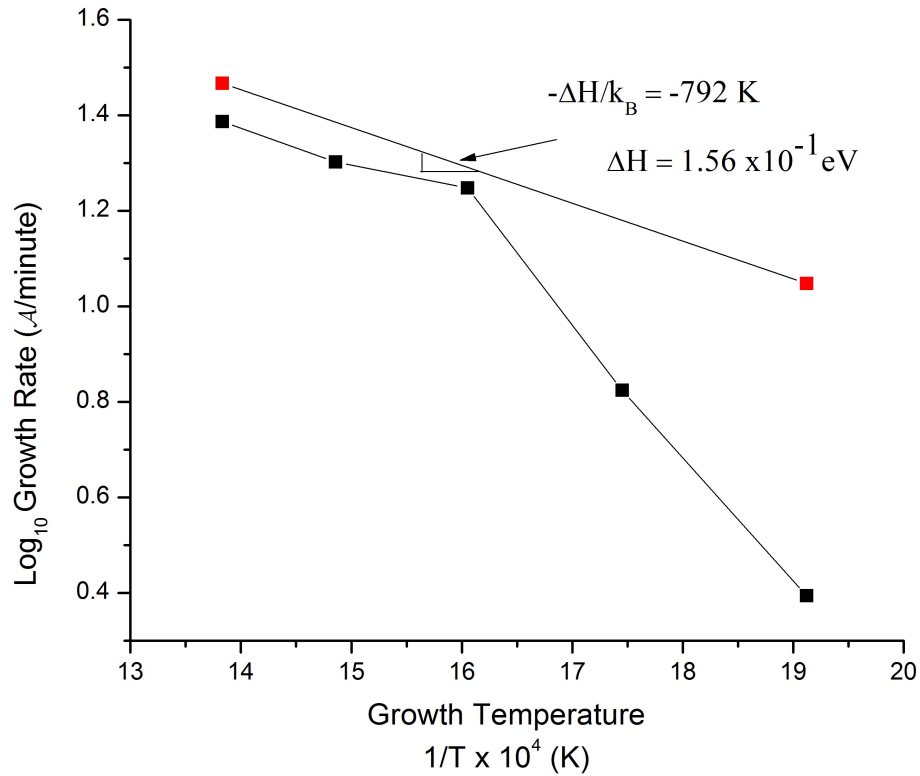
Fig 9: Arrhenius plot of pyrite thin film growth rate vs growth temperature for three-step growths. Linear fits are used to calculate enthalpy of formation (ΔH) for two apparent trends.

In films grown using a three-step process, where a seed layer was grown at low temperature followed by growth at high temperature and then finished with a low temperature capping layer, three distinctly different grain morphologies are observed in the TEM images. Fig 10-1 displays an example of a three-step growth, during which the seed layer is formed at 250°C, the high temperature layer is formed at 400°C and the capping layer is formed at 250°C. The Initial layers formed at low temperature contain small grains with flat tops or rounded tops. On top of them, columnar grains formed during the high temperature growth process. For both of

these layers, the widths of the grains range from ~10-30 nm. The low temperature capping layer also has small grains with flat or rounded tops, similar to those observed in the low temperature seed layer(Fig 10-1). As Fig 7 shows, both one-step and three-step growths processes result in a growth rate that increases with increasing growth temperature. As the substrates cool, deposition during cool down may be considered part of the capping layer.

The grains of the seed layer formed in the three-step process do not coalesce into larger grains during the high temperature growth step. The use of a low temperature seed layer preceding the high temperature growth process, in general, results in small grains and does not produce a desirable film morphology.

In films grown using a one-step constant substrate temperature process, a columnar morphology is apparent throughout the thickness of the pyrite layer. For substrate temperatures of 250°C, the grains are approximately 10-30 nm wide (Fig 10-2 B). For substrate temperatures of 400°C, the grains are approximately 70-100 nm wide (Fig 10-2 C). In these films, the average grain size increases with increasing substrate temperature. While a rough surface is found in the films with the larger grains, it may be possible to smooth this rough surface with the use of a lower temperature capping layer.

Fig 10-1: TEM cross sections of three-step grown pyrite thin films displaying micro-structural characteristics. A) Film grown using a three-step process at 250-400-250˚C, shown at 20,000x magnification.
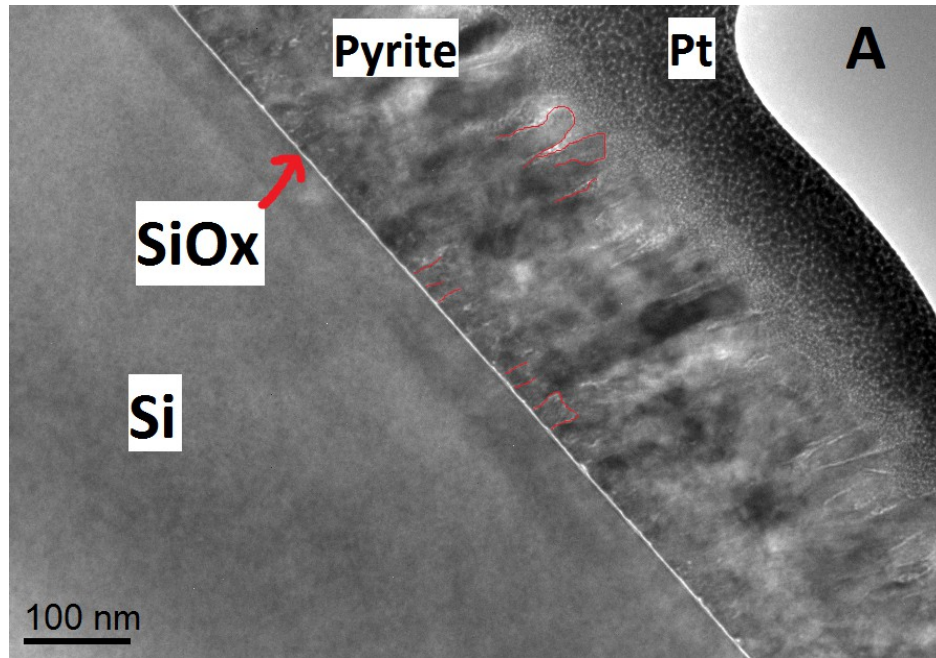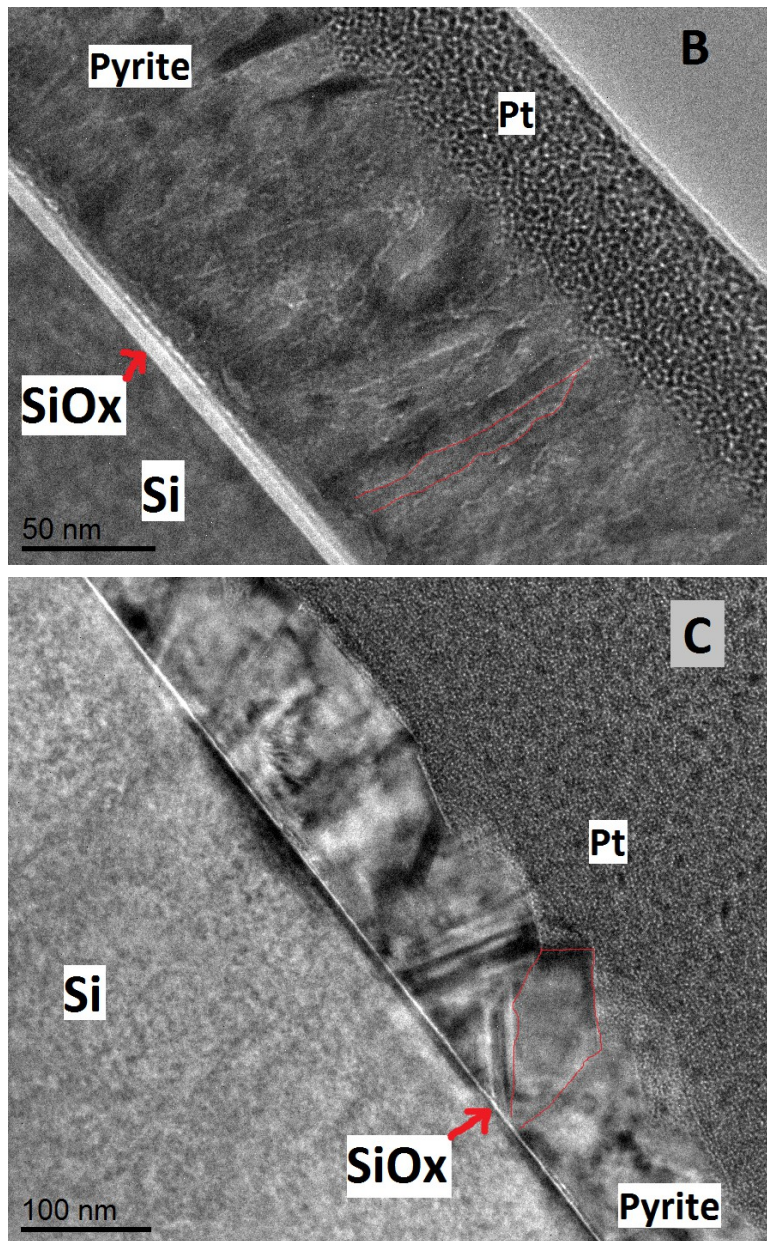
Fig 10-2: TEM cross sections of one-step grown pyrite thin films displaying micro-structural characteristics. B) Film grown using a one-step process at 250˚C, shown at 60,000x magnification. C) Film grown using a one-step process at 400˚C, shown at 30,000x magnification.

ELECTRICAL CHARACTERIZATION

For all samples studied, the resistivities, inferred from current-voltage measurements and RBS measurements of film thickness, shows an increase in resistivity with decreasing temperature, as is characteristic of a semiconductor with a carrier concentration on the insulator side of the metal-insulator transition (Fig 12). Therefore it is reasonable to assume that their carrier concentration is on the order of 10^{19} cm^{-3} or less. Hall effect measurements were performed using equipment with a lower detection limit of ~0.1 cm^2/Vs. A measurable Hall voltage was not observed, indicating that the carrier mobility is less than ~0.1 cm^2/Vs. Altermatt et al has plotted experimental values of mobility for bulk synthetic and natural pyrite. From that graph, we would expect high-quality low-contamination pyrite with carrier concentrations of ~10^{19} cm^{-3} to have mobilities on the order of ~8 cm^2/Vs or less(Fig 11) [3]. Lower than expected mobilities result from the presence of additional scattering sites, which arises from compensation by native and/or impurity point defects.
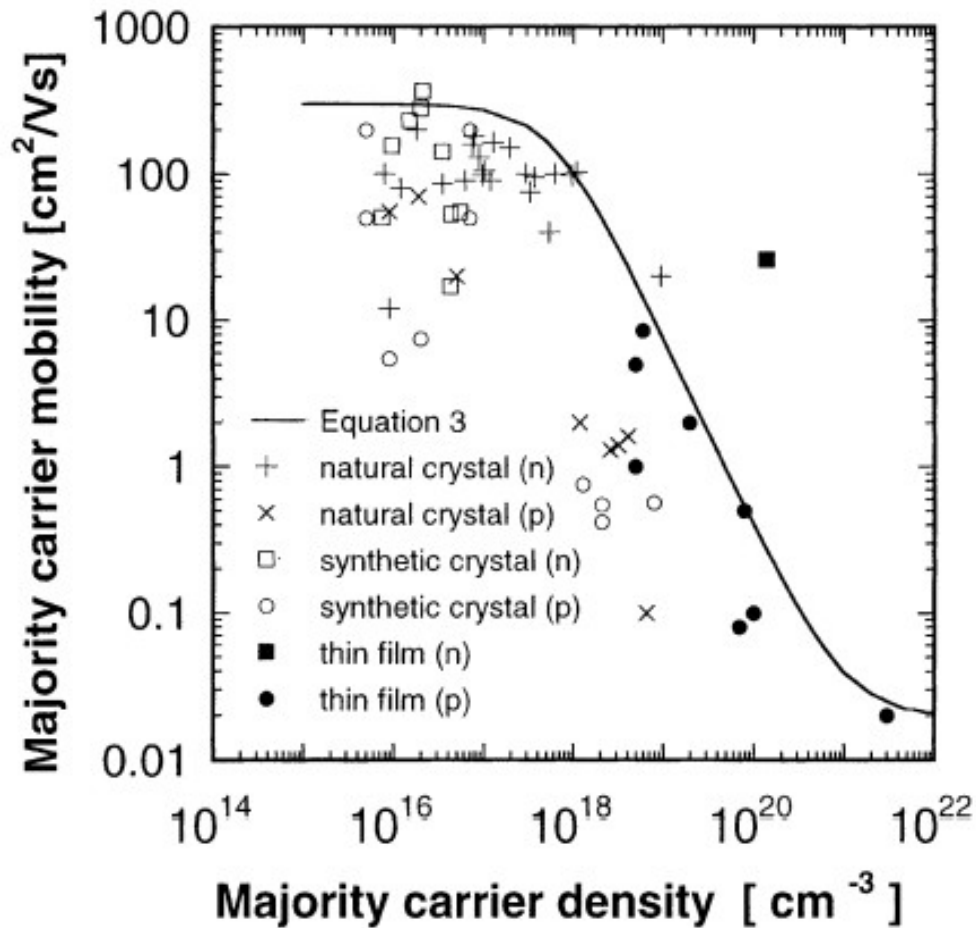
Figure 11: Calculated and experimentally measured mobilities in pyrite thin films as a function of dopant concentration [3].

S becomes extremely reactive at metal surfaces exceeding 260ºC [14]. Since many S-compounds are volatile at our growth temperature, contamination in the pyrite thin films introduced during growth is expected. Secondary-ion mass spectroscopy (SIMS) results (Table 1) confirmed this. Many of the contaminants detected in our films are present in stainless steels, particularly Cr, Mn, Si, and Ni.
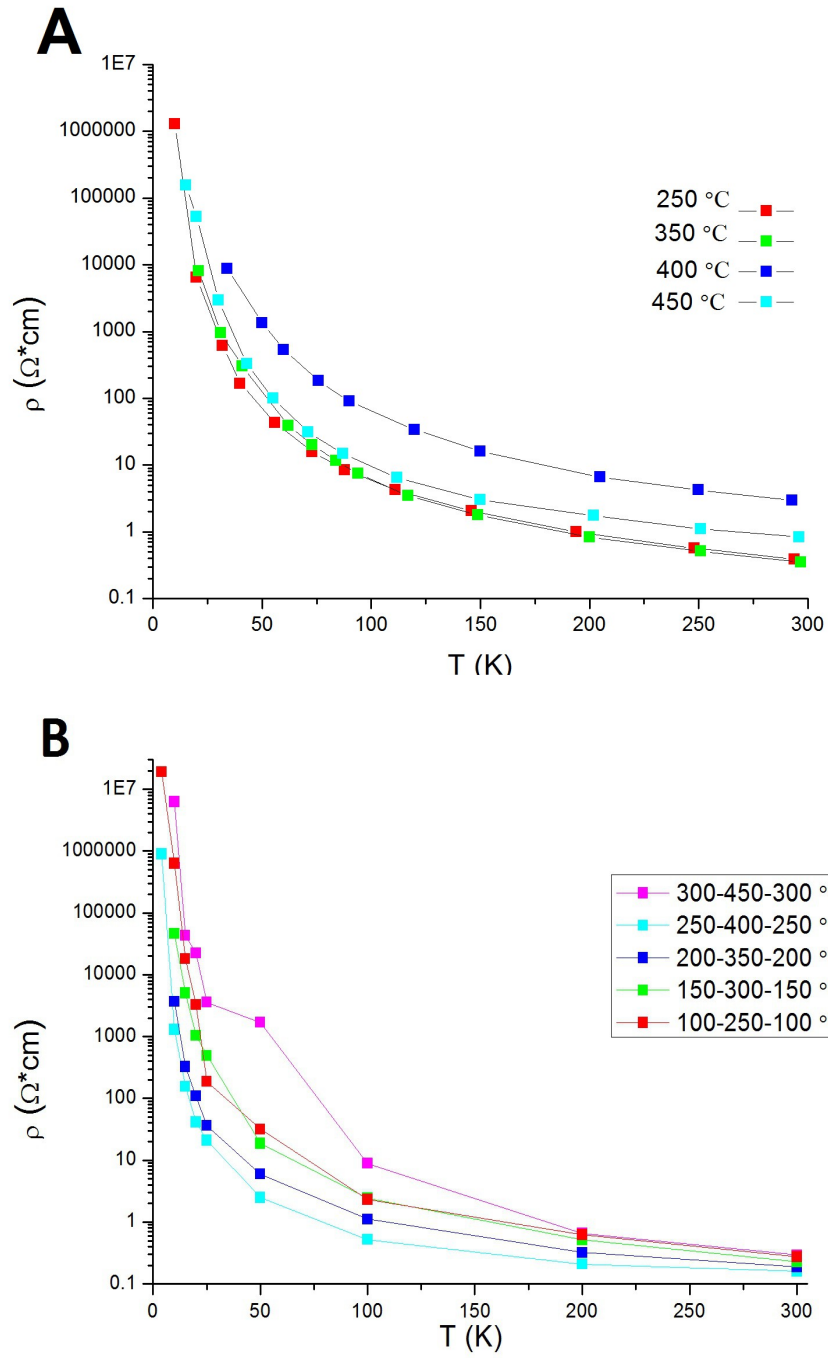
Figure 12: Resistivity versus temperature for: A) one-step and B) three-step pyrite thin films.

During my work with our sequential evaporation chamber I have observed the reaction of S with many types of materials used in the chamber. Cu components, including UHV flange gaskets and power feed-throughs used to power heating coax cables, in particular react with S at room temperature, and form a corroded outer layer in less than 24 hours.

I carried out experiments to identify vacuum compatible materials that would be nonreactive or minimally reactive in the corrosive S-environment. Stainless steel components which are subject to elevated temperatures, such as the substrate heater and S crucible also react heavily with S gas (Fig 13). Inconel, an alloy designed to resist oxidation and corrosion at high temperatures, acts as a protective sheath for the Thermocoax heating wire used in the substrate heater and S crucible. This material also corrodes in the SE chamber. (Fig 13)

Element	Concentration (cm^{-3})	ppm
Ni	1.20E+20	2404
Si	3.80E+19	773
Mg	2.90E+19	595
Mn	1.50E+19	311
Pb	1.30E+19	270
Cr	9.30E+18	188
W	7.10E+18	143
Ca	4.90E+18	100

Table 1: Contaminants detected by SIMS in three-step pyrite thin film grown at 300-450-300 °C.

Figure 13: Examples of corroded UHV chamber components. Left: remnants of Cu power-feedthrough after ~6 months of use. Center: Corroded UHV flange Cu gaskets after <24 hours at room temperature in SE chamber. Right: stainless steel substrate heater; 1) corroded stainless steel sheet metal, 2) inconel sheath of heating element, 3) exposed MgO powder insulation as a result of corrosion damage to inconel sheath. Bottom: Grooved tracks in rotating substrate heater, indicating that metal is being removed by corrosion.

CONCLUSIONS

I have carried out a systematic study of pyrite growth using sequential evaporation to investigate the effects of growth temperature on the grain morphology, structural, chemical and electrical properties of pyrite thin films. Polycrystalline films were found to have narrower XRD peak widths, and thus improved crystalline quality at higher growth temperatures. The Fe sticking coefficients and pyrite growth rates increase monotonically with growth temperature, indicating that these parameters are thermally activated processes. Resistivity of thin films sharply increases at low temperatures, indicating that majority carrier concentration is on the insulator side of the metal-insulator transition, which is expected to be in the range of $\sim 10^{19}$ cm^{-3}. The low observed mobilities indicate that the materials are strongly compensated. SIMS measurements verify that the total impurity concentration in a typical film exceeds 10^{20} cm^{-3}. Contaminants are likely due to material corrosion from reaction with S gas at high temperature. A second generation chamber must be built to address the issue of contamination by utilizing materials which will not corrode and potentially introduce metal-sulfides into films.

FUTURE WORK

The hostile chemical environment in the sequential evaporation chamber poses a number of challenges and limitations. Electrical connections which utilize Cu will degrade and eventually break, leading to the unexpected loss of a growth experiment. The degradation of the inconel sheath around the heating wire often leads to unexpected shorts and ultimately the need for replacement of the heating wire. The realization and construction of a second generation SE chamber will bring with it the capability of producing pyrite thin films with less impurity defects. For a next generation SE chamber, materials must be selected carefully for key components. To assess which materials may be viable solutions I have observed the results of subjecting samples of various materials to S pressures up to 1 atmosphere at temperatures exceeding 500ºC for periods of days to weeks. These material S-corrosion tests show two main candidates for

26

corrosion resistant components; Macor, a machinable glass-ceramic produced by Corning, and Al metal. The substrate heater requires machinable materials that can reach elevated temperatures and not react with S gas. For this application, I would suggest that Macor be used when possible, because of its high temperature stability and resistance to corrosion. For electrical wires, electrical connections and gaskets, Al may be used so long as temperatures will not exceed the melting point of 660ºC. In addition I have found solid Fe wire to be able to withstand the corrosive environment for a limited time and could also be used for wires and electrical connections.

The first goal would be to synthesize single-step films at varying substrate temperatures and compare their impurity concentrations with that of films grown in the current SE chamber. Work should be done to determine any remaining sources for contamination and eliminate them wherever possible. It was shown that crystal quality improves and grain size increases with increasing substrate temperatures, therefore growth experiments should be conducted at temperatures as high as the predicted thermodynamically stable region for pyrite (743ºC). If high-quality structural and stoichiometric single-phase films can be fabricated, high mobilities of 100-200 cm^2/Vs should be achievable in undoped films. Experiments should then be done to see if pyrite films can be successfully doped n-type with Co and Ni as well as p-type by doping with As, as these are well established pyrite dopants [15]. It is theorized that group 7 elements may be able to act as n-type dopants in pyrite [16]. Experiments should be done to determine if doping with group 7 elements produces n-type films.

As I suggested, a possible mechanism for the low Fe sticking at lower growth temperatures suggests that a volatile Fe-containing species is desorbing during growth. The use of an RGA, in combination with pulsed evaporation of Fe, could be used during synthesis to determine the residence time and activation energy of the Fe-containing desorbing species for a wide range of growth conditions. A witness sample that is later characterized with RBS may be

27

placed outside of the substrate heater to monitor the relative amounts of Fe being deposited.

REFERENCES

1.   Ellabban, O., H. Abu-Rub, and F. Blaabjerg, *Renewable energy resources: Current status, future prospects and their enabling technology.* Renewable and Sustainable Energy Reviews, 2014. **39**(0): p. 748-764.

2.   Wadia, C., A.P. Alivisatos, and D.M. Kammen, *Materials Availability Expands the Opportunity for Large-Scale Photovoltaics Deployment.* Environmental Science & Technology, 2009. **43**(6): p. 2072-2077.

3.   Altermatt, P.P., et al., *Specifying targets of future research in photovoltaic devices containing pyrite (FeS$_2$) by numerical modelling.* Solar Energy Materials and Solar Cells, 2002. **71**(2): p. 181-195.

4.   Bi, Y., et al., *Air Stable, Photosensitive, Phase Pure Iron Pyrite Nanocrystal Thin Films for Photovoltaic Application.* Nano Letters, 2011. **11**(11): p. 4953-4957.

5.   Höpfner, C., et al., *Stoichiometry-, phase- and orientation-controlled growth of polycrystalline pyrite (FeS$_2$) thin films by MOCVD.* Journal of Crystal Growth, 1995. **151**(3-4): p. 325-334.

6.   Thomas, B., et al., *Formation of secondary iron-sulfur phases during the growth of polycrystalline iron pyrite (FeS$_2$) thin films by MOCVD.* Journal of Materials Science: Materials in Electronics, 1998. **9**(1): p. 61-64.

7.   Thomas, B., et al., *Growth of FeS$_2$ (pyrite) thin films on single crystalline substrates by low pressure metal-organic chemical vapor deposition.* Journal of Crystal Growth, 1995. **146**(1-4): p. 630-635.

8.   Birkholz, M., et al., *Sputtering of thin pyrite films.* Solar Energy Materials and Solar Cells, 1992. **27**(3): p. 243-251.

9.   Bronold, M., et al., *Thin pyrite (FeS$_2$) films by molecular beam deposition.* Thin Solid Films, 1997. **304**(1-2): p. 178-182.

10.   Vahidi, M., et al., *Growth of epitaxial pyrite (FeS$_2$) thin films using sequential evaporation.* Acta Materialia, 2013. **61**(19): p. 7392-7398.

11.   Toulmin, P.I. and P.B.J. Barton, *A thermodynamic study of pyrite and pyrrhotite.* Geochimica et Cosmochimica Acta, 1964. **28**: p. 641-671.

12.   Barker, W.W. and T.C. Parks, *The thermodynamic properties of pyrrhotite and pyrite: A re-evaluation.* Geochimica et Cosmochimica Acta, 1986. **50**(10): p. 2185-2194.

13.   Kullerud, G. and H.S. Yoder, *Pyrite stability relations in the FeS-S system.* Economic Geology, 1959. **54**(4): p. 533-572.

14.   Meyer, B., *Elemental Sulfur.* Chemical Reviews, 1976. **76**(3): p. 367-388.

15.   Lehner, S.W., et al., *Defect energy levels and electronic behavior of Ni-, Co-, and As-doped synthetic pyrite (FeS$_2$).* Journal of Applied Physics, 2012. **111**(8): p. 083717-8.

16.   Siebert, D., et al., *An ESR investigation of synthetic pyrite crystals.* Zeitschrift fur Naturforschung. Teil A, Physik, physikalische Chemie, Kosmophys, 1989. **44a**: p. 59-66.